

Improved calorimetric particle identification in NA62 using machine learning techniques

The NA62 Collaboration

Abstract

Measurement of the ultra-rare $K^+ \rightarrow \pi^+ \nu \bar{\nu}$ decay at the NA62 experiment at CERN requires high-performance particle identification to distinguish muons from pions. Calorimetric identification currently in use, based on a boosted decision tree algorithm, achieves a muon misidentification probability of 1.2×10^{-5} for a pion identification efficiency of 75% in the momentum range of 15–40 GeV/ c . In this work, calorimetric identification performance is improved by developing an algorithm based on a convolutional neural network classifier augmented by a filter. Muon misidentification probability is reduced by a factor of six with respect to the current value for a fixed pion-identification efficiency of 75%. Alternatively, pion identification efficiency is improved from 72% to 91% for a fixed muon misidentification probability of 10^{-5} .

The NA62 Collaboration

Université Catholique de Louvain, Louvain-La-Neuve, Belgium

E. Cortina Gil¹, A. Kleimenova¹, E. Minucci², S. Padolski³, P. Petrov, A. Shaikhiev⁴, R. Volpe⁵

TRIUMF, Vancouver, British Columbia, Canada

W. Fedorko, T. Numao, Y. Petrov, B. Velghe*, V. W. S. Wong, M. Yu

University of British Columbia, Vancouver, British Columbia, Canada

D. Bryman⁶, J. Fu

Charles University, Prague, Czech Republic

Z. Hives, T. Husek⁷, J. Jerhot⁸, K. Kampf, M. Zamkovsky⁹

Institut für Physik and PRISMA Cluster of Excellence, Universität Mainz, Mainz, Germany

A.T. Akmete, R. Aliberti¹⁰, G. Khoriali¹¹, J. Kunze, D. Lomidze¹², L. Peruzzo, M. Vormstein, R. Wanke

Dipartimento di Fisica e Scienze della Terra dell'Università e INFN, Sezione di Ferrara, Ferrara, Italy

P. Dalpiaz, M. Fiorini, I. Neri, A. Norton¹³, F. Petrucci, M. Soldani, H. Wahl¹⁴

INFN, Sezione di Ferrara, Ferrara, Italy

L. Bandiera, A. Cotta Ramusino, A. Gianoli, A. Mazzolari, M. Romagnoni, A. Sytov

Dipartimento di Fisica e Astronomia dell'Università e INFN, Sezione di Firenze, Sesto Fiorentino, Italy

E. Iacopini, G. Latino, M. Lenti, P. Lo Chiatto, I. Panichi, A. Parenti

INFN, Sezione di Firenze, Sesto Fiorentino, Italy

A. Bizzeti¹⁵, F. Bucci

Laboratori Nazionali di Frascati, Frascati, Italy

A. Antonelli, G. Georgiev¹⁶, V. Kozhuharov¹⁶, G. Lanfranchi, S. Martellotti, M. Moulson, T. Spadaro, G. Tinti

Dipartimento di Fisica "Ettore Pancini" e INFN, Sezione di Napoli, Napoli, Italy

F. Ambrosino, T. Capussela, M. Corvino, M. D'Errico, D. Di Filippo, R. Fiorenza¹⁷, R. Giordano, P. Massarotti, M. Mirra, M. Napolitano, G. Saracino

Dipartimento di Fisica e Geologia dell'Università e INFN, Sezione di Perugia, Perugia, Italy

G. Anzivino, F. Brizioli⁹, E. Imbergamo, R. Lollini, R. Piandani¹⁸, C. Santoni

INFN, Sezione di Perugia, Perugia, Italy

M. Barbanera, P. Cenci, B. Checcucci, P. Lubrano, M. Lupi¹⁹, M. Pepe, M. Piccini

Dipartimento di Fisica dell'Università e INFN, Sezione di Pisa, Pisa, Italy
F. Costantini¹⁴, L. Di Lella¹⁴, N. Doble¹⁴, M. Giorgi, S. Giudici, G. Lamanna,
E. Lari, E. Pedreschi, M. Sozzi

INFN, Sezione di Pisa, Pisa, Italy
C. Cerri, R. Fantechi, L. Pontisso²⁰, F. Spinella

Scuola Normale Superiore e INFN, Sezione di Pisa, Pisa, Italy
I. Mannelli

Dipartimento di Fisica, Sapienza Università di Roma e INFN, Sezione di Roma I, Roma, Italy
G. D'Agostini, M. Raggi

INFN, Sezione di Roma I, Roma, Italy
A. Biagioni, P. Cretaro, O. Frezza, E. Leonardi, A. Lonardo, M. Turisini, P. Valente,
P. Vicini

INFN, Sezione di Roma Tor Vergata, Roma, Italy
R. Ammendola, V. Bonaiuto²¹, A. Fucci, A. Salamon, F. Sargeni²²

Dipartimento di Fisica dell'Università e INFN, Sezione di Torino, Torino, Italy
R. Arcidiacono²³, B. Bloch-Devaux, M. Boretto⁹, E. Menichetti, E. Migliore, D. Soldi

INFN, Sezione di Torino, Torino, Italy
C. Biino, A. Filippi, F. Marchetto

Instituto de Física, Universidad Autónoma de San Luis Potosí, San Luis Potosí, Mexico
A. Briano Olvera, J. Engelfried, N. Estrada-Tristan²⁴, M. A. Reyes Santos²⁴

Horia Hulubei National Institute for R&D in Physics and Nuclear Engineering, Bucharest-Magurele, Romania
P. Boboc, A. M. Bragadireanu, S. A. Ghinescu, O. E. Hutanu

Faculty of Mathematics, Physics and Informatics, Comenius University, Bratislava, Slovakia
L. Bician²⁵, T. Blazek, V. Cerny, Z. Kucerova⁹

CERN, European Organization for Nuclear Research, Geneva, Switzerland
J. Bernhard, A. Ceccucci, H. Danielsson, N. De Simone²⁶, F. Duval, B. Döbrich²⁷,
L. Federici, E. Gamberini, L. Gatignon²⁸, R. Guida, F. Hahn[†], E. B. Holzer,
B. Jenninger, M. Koval²⁵, P. Laycock³, G. Lehmann Miotto, P. Lichard, A. Mapelli,
R. Marchevski¹, K. Massri²⁸, M. Noy, V. Palladino, M. Perrin-Terrin^{29, 30},
J. Pinzino³¹, V. Ryjov, S. Schuchmann, S. Venditti

School of Physics and Astronomy, University of Birmingham, Birmingham, United Kingdom

T. Bache¹, M. B. Brunetti³², V. Duk⁵, V. Fascianelli³³, J. R. Fry, F. Gonnella, E. Goudzovski, J. Henshaw, L. Iacobuzio, C. Lazzeroni, N. Lurkin⁸, F. Newson, C. Parkinson, A. Romano, J. Sanders, A. Sergi³⁴, A. Sturges, J. Swallow⁹, A. Tomczak

School of Physics, University of Bristol, Bristol, United Kingdom

H. Heath, R. Page, S. Trilov

School of Physics and Astronomy, University of Glasgow, Glasgow, United Kingdom

B. Angelucci, D. Britton, C. Graham, D. Protopopescu

Faculty of Science and Technology, University of Lancaster, Lancaster, United Kingdom

J. Carmignani³⁵, J. B. Dainton, R. W. L. Jones, G. Ruggiero³⁶

School of Physical Sciences, University of Liverpool, Liverpool, United Kingdom

L. Fulton, D. Hutchcroft, E. Maurice³⁷, B. Wrona

Physics and Astronomy Department, George Mason University, Fairfax, Virginia, USA

A. Conovaloff, P. Cooper, D. Coward³⁸, P. Rubin

Authors affiliated with an Institute or an international laboratory covered by a cooperation agreement with CERN

A. Baeva, D. Baigarashev³⁹, D. Emelyanov, T. Enik, V. Falaleev⁵, S. Fedotov, K. Gorshakov, E. Gushchin, V. Kekelidze, D. Kereibay, S. Kholodenko, A. Khotyantsev, A. Korotkova, Y. Kudenko, V. Kurochka, V. Kurshetsov, L. Litov¹⁶, D. Madigozhin, M. Medvedeva, A. Mefodev, M. Misheva⁴⁰, N. Molokanova, S. Movchan, V. Obraztsov, A. Okhotnikov, A. Ostankov[†], I. Polenkevich, Yu. Potrebenikov, A. Sadovskiy, V. Semenov[†], S. Shkarovskiy, V. Sugonyaev, O. Yushchenko, A. Zinchenko[†]

* Corresponding author: B. Velghe, email: bvelghe@triumf.ca

[†] Deceased

¹Present address: Ecole Polytechnique Fédérale Lausanne, CH-1015 Lausanne, Switzerland

²Present address: Syracuse University, Syracuse, NY 13244, USA

³Present address: Brookhaven National Laboratory, Upton, NY 11973, USA

⁴Present address: School of Physics and Astronomy, University of Birmingham, Birmingham, B15 2TT, UK

⁵Present address: INFN, Sezione di Perugia, I-06100 Perugia, Italy

⁶Also at TRIUMF, Vancouver, British Columbia, V6T 2A3, Canada

⁷Present address: Department of Astronomy and Theoretical Physics, Lund University, Lund, SE 223-62, Sweden

⁸Present address: Université Catholique de Louvain, B-1348 Louvain-La-Neuve, Belgium

⁹Present address: CERN, European Organization for Nuclear Research, CH-1211 Geneva 23, Switzerland

¹⁰Present address: Institut für Kernphysik and Helmholtz Institute Mainz, Universität Mainz,

Mainz, D-55099, Germany

¹¹Present address: Universität Würzburg, D-97070 Würzburg, Germany

¹²Present address: European XFEL GmbH, D-22761 Hamburg, Germany

¹³Present address: School of Physics and Astronomy, University of Glasgow, Glasgow, G12 8QQ, UK

¹⁴Present address: Institut für Physik and PRISMA Cluster of Excellence, Universität Mainz, D-55099 Mainz, Germany

¹⁵Also at Dipartimento di Scienze Fisiche, Informatiche e Matematiche, Università di Modena e Reggio Emilia, I-41125 Modena, Italy

¹⁶Also at Faculty of Physics, University of Sofia, BG-1164 Sofia, Bulgaria

¹⁷Present address: Scuola Superiore Meridionale e INFN, Sezione di Napoli, I-80138 Napoli, Italy

¹⁸Present address: Instituto de Física, Universidad Autónoma de San Luis Potosí, 78240 San Luis Potosí, Mexico

¹⁹Present address: Institut am Fachbereich Informatik und Mathematik, Goethe Universität, D-60323 Frankfurt am Main, Germany

²⁰Present address: INFN, Sezione di Roma I, I-00185 Roma, Italy

²¹Also at Department of Industrial Engineering, University of Roma Tor Vergata, I-00173 Roma, Italy

²²Also at Department of Electronic Engineering, University of Roma Tor Vergata, I-00173 Roma, Italy

²³Also at Università degli Studi del Piemonte Orientale, I-13100 Vercelli, Italy

²⁴Also at Universidad de Guanajuato, 36000 Guanajuato, Mexico

²⁵Present address: Charles University, 116 36 Prague 1, Czech Republic

²⁶Present address: DESY, D-15738 Zeuthen, Germany

²⁷Present address: Max-Planck-Institut für Physik (Werner-Heisenberg-Institut), München, D-80805, Germany

²⁸Present address: Faculty of Science and Technology, University of Lancaster, Lancaster, LA1 4YW, UK

²⁹Present address: Aix Marseille University, CNRS/IN2P3, CPPM, F-13288, Marseille, France

³⁰Also at Université Catholique de Louvain, B-1348 Louvain-La-Neuve, Belgium

³¹Present address: INFN, Sezione di Pisa, I-56100 Pisa, Italy

³²Present address: Department of Physics, University of Warwick, Coventry, CV4 7AL, UK

³³Present address: Center for theoretical neuroscience, Columbia University, New York, NY 10027, USA

³⁴Present address: Dipartimento di Fisica dell'Università e INFN, Sezione di Genova, I-16146 Genova, Italy

³⁵Present address: School of Physical Sciences, University of Liverpool, Liverpool, L69 7ZE, UK

³⁶Present address: Dipartimento di Fisica e Astronomia dell'Università e INFN, Sezione di Firenze, I-50019 Sesto Fiorentino, Italy

³⁷Present address: Laboratoire Leprince Ringuet, F-91120 Palaiseau, France

³⁸Also at SLAC National Accelerator Laboratory, Stanford University, Menlo Park, CA 94025, USA

³⁹Also at L.N. Gumilyov Eurasian National University, 010000 Nur-Sultan, Kazakhstan

⁴⁰Present address: Institute of Nuclear Research and Nuclear Energy of Bulgarian Academy of Science (INRNE-BAS), BG-1784 Sofia, Bulgaria

1 Introduction

The NA62 experiment at CERN is dedicated to measurements of charged kaon decays, including the highly-suppressed “golden mode” $K^+ \rightarrow \pi^+ \nu \bar{\nu}$ [1] with a Standard Model branching ratio of $(8.4 \pm 1.0) \times 10^{-11}$ [2]. Background suppression requires a μ^+ misidentification probability below 10^{-7} , which is achieved by a combination of calorimetric and Cherenkov π^+ identification.

Machine learning (ML) methods developed primarily for image recognition can be applied to particle identification (PID) at NA62. Convolutional neural networks (CNN), a type of deep neural network, have been successfully used for classification tasks commonly encountered in particle physics [3, 4, 5]. In this work, a calorimetric PID algorithm based on ML models is designed for the NA62 experiment. Two ML models are considered: LightGBM [6], which is an implementation of a gradient boosting machine (GBM) [7], and a CNN-based model. Performance of the algorithm is compared to that of the boosted decision tree (BDT) implemented using TMVA GradientBoost [8], currently used by NA62.

2 NA62 beam and detector

The layout of the NA62 detector [9] is shown schematically in Fig. 1. An unseparated secondary beam of π^+ (70%), protons (23%), and K^+ (6%) is created by directing 400 GeV/ c protons extracted from the CERN SPS onto a beryllium target in spills of 3 s effective duration. The central beam momentum is 75 GeV/ c , and the momentum spread is 1% (rms). Beam kaons are tagged with 70 ps time resolution by a differential Cherenkov counter (KTAG) using a nitrogen gas radiator at 1.75 bar pressure contained in a 5 m long vessel. Beam particle positions, momenta and times are measured by a silicon pixel spectrometer consisting of three stations (GTK1, 2, 3) and four dipole magnets. A 1.2 m thick steel collimator (COL) is placed upstream of GTK3 to absorb hadrons produced in upstream K^+ decays. Inelastic interactions of beam particles in the GTK are detected by an array of scintillator hodoscopes (CHANTI). The beam is delivered into a vacuum tank evacuated to a pressure of 10^{-6} mbar, which contains a 75 m long fiducial decay volume (FV) starting 2.6 m downstream of GTK3.

Downstream of the FV, undecayed beam particles continue their path in vacuum. Momenta of charged particles produced in K^+ decays in the FV are measured by a magnetic spectrometer (STRAW) located in the vacuum tank downstream of the FV. The spectrometer consists of four tracking chambers made of straw tubes, and a dipole magnet located between the the second and third chambers that provides a horizontal momentum kick of 270 MeV/ c . The spectrometer momentum resolution is $\sigma_p/p = (0.30 \oplus 0.005 \cdot p)\%$, where the momentum p is expressed in GeV/ c .

A ring-imaging Cherenkov detector (RICH), consisting of a 17.5 m long vessel filled with neon at atmospheric pressure (with a Cherenkov threshold for pions of 12.5 GeV/ c), is used for the identification of charged particles and for time measurement with 70 ps precision. Two scintillator hodoscopes (CHOD) located downstream of the RICH provide trigger signals and time measurements with 200 ps precision.

A quasi-homogeneous liquid-krypton (LKr) electromagnetic calorimeter of thickness 27 radiation lengths is used for particle identification and photon detection. The calorimeter has an active volume of 7 m³, is segmented in the transverse plane into 13248 projective cells of 2×2 cm², and provides an energy resolution $\sigma_E/E = (4.8/\sqrt{E} \oplus 11/E \oplus 0.9)\%$, where E is expressed in GeV. To achieve hermetic acceptance for photons emitted in the FV by K^+ decays at angles up to 50 mrad to the beam axis, the LKr calorimeter is supplemented by annular lead glass detectors (LAV) installed in 12 positions inside and downstream of the vacuum tank, and two lead/scintillator sampling calorimeters (IRC, SAC) located close to the beam axis.

A steel/scintillator hadronic sampling calorimeter is formed of two modules (MUV1, 2) with transverse dimensions of approximately 2.6×2.6 m². The MUV1 (MUV2) module consists

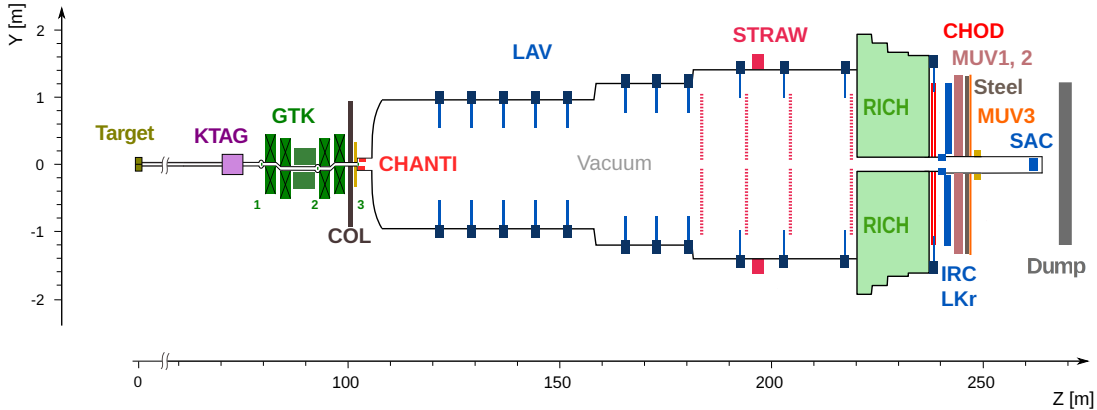


Figure 1: Schematic side view of the NA62 detector used in 2018.

of 24 steel plates of 26.8 (25) mm thickness, interleaved with 9 (4.5) mm thick scintillator layers, resulting in a total thickness of 4.1 (3.7) interaction lengths. The scintillator layers in both modules are made of strips aligned alternately in the horizontal and vertical directions in consecutive planes. Each MUV1 scintillator layer consists of 48 strips, including 40 strips spanning the entire transverse length of the detector (read out at both ends), and 8 central strips of half-length (read out at the peripheral end), leading to 2×44 channels per plane. Each MUV2 scintillator layer consists of 2×22 strips, each spanning half the transverse length and read out at the peripheral end. In both modules, all strips located in the same transverse position in different layers are coupled to the same photomultiplier, thus providing a horizontal and a vertical view. A muon detector (MUV3) is located behind a 80 cm (4.8 interaction lengths) thick iron wall, has a transverse size of $2.64 \times 2.64 \text{ m}^2$, and is built from 50 mm thick scintillator tiles, including 140 regular tiles of $220 \times 220 \text{ mm}^2$ transverse dimensions, and eight smaller central tiles adjacent to the beam pipe.

A two-level trigger system [10, 11] is employed to reduce the event rate from 10 MHz to about 100 kHz. Multiple trigger lines with different downscaling factors are operated concurrently.

3 GBM and CNN algorithms

Supervised ML algorithms are used to construct a function (called *model* or *classifier*), $f(x_i; \theta)$, mapping a set of inputs x_i (called *examples*) consisting of a number of attributes (called *features*) to a set of outputs y_i (called *labels*). The set of model parameters, θ , is chosen to minimise a *loss function* (also called *objective function*), $\mathcal{L} = \sum_i \ell(y_i, f(x_i; \theta))$, where the function $\ell(y, f(x; \theta))$ is selected depending on the problem to solve [12, 13].

GBM is a generic family of algorithms used to build strongly predictive classifiers as linear combinations of *weak* classifiers (such as decision trees). The classifier, $f(x_i)$, is constructed iteratively, starting from an initial decision tree. At each step m , residuals are computed using the loss function obtained at the previous step as $-\partial \ell(y_i, f_{m-1}(x_i)) / \partial f_{m-1}$, and a regression tree fitting the residuals is constructed and added to the linear combination. This procedure is repeated until a stopping condition is met [7].

CNN algorithms have been developed to address computer vision tasks such as translation-invariant image classification, and can recognize complex geometric features at multiple scales. CNNs consist of consecutive *layers*, the output of each layer being the input to the next one. Each layer is represented by a function $g(x)$, where x is an input tensor. Common layer types include convolutional, batch normalisation and pooling layers [12, 13]. It has been observed [14]

that increasing the number of layers leads to degradation of the training performance; to mitigate this issue, the ResNet architecture [14] introduces groups of consecutive layers called the *residual blocks*. Instead of learning the parameters of the underlying function $g(x)$ directly, the block learns the parameters of the residual function $g_r(x)$, encoding the difference between the input and output of the layer. Many of these blocks are typically stacked.

4 Data samples

Two independent datasets are employed: a *training and validation dataset* is used to train the models and adjust the hyperparameters (i.e. the parameters not derived via training), while an independent *test dataset* is used to characterise the performance of the optimal model with a frozen set of hyperparameters. The training and validation (test) dataset is based on 2.5% (1.5%) of the data sample collected by the NA62 experiment in 2016–2018. The training and validation dataset contains events collected with a non-downscaled $K^+ \rightarrow \pi^+\nu\bar{\nu}$ trigger line [1] based on RICH and CHOD signals in the absence of in-time MUV3 signals, and a control trigger line based on the CHOD signal downscaled by a factor of 400. The test dataset contains events collected with the control trigger line. This provides sufficient statistics for training, ensuring that the test dataset is free from trigger-induced bias.

High-purity pion (π^+), muon (μ^+) and positron (e^+) track samples in the momentum range 15–50 GeV/ c are obtained from $K^+ \rightarrow \pi^+\pi^0$, $K^+ \rightarrow \mu^+\nu$ and $K^+ \rightarrow \pi^0e^+\nu$ decay candidates selected without calorimetric particle identification, following the procedure used earlier for the existing NA62 BDT algorithm. Isolated STRAW tracks with associated in-time KTAG, CHOD, RICH and LKr signals and a single associated GTK track are considered. The decay vertex, reconstructed as the point of closest approach of the STRAW and GTK tracks, is required to be located in the FV and within the beam envelope. For the $K^+ \rightarrow \pi^+\pi^0$ and $K^+ \rightarrow \pi^0e^+\nu$ decays, a prompt $\pi^0 \rightarrow \gamma\gamma$ decay is reconstructed by measuring the photons in the LKr calorimeter. Further selection criteria are based on photon veto conditions, particle identification in the RICH, and missing mass squared, $m_{\text{miss}}^2 = (P_K - P_{\text{tr}})^2$, where P_K and P_{tr} are the K^+ and decay track four-momenta, respectively. A label (π^+ , μ^+ or e^+) is assigned to each selected track.

The following features are encoded as matrices and vectors: track momentum and impact position in the LKr front plane; presence of a matching MUV3 signal; energy deposits in a matrix of 22×22 LKr calorimeter cells centered around the track impact position (these matrices are sparse due to the LKr Molière radius of 4.7 cm); total LKr energy deposit associated to the track; energy deposits in the horizontal and vertical views in all MUV1 channels (2×44 channels in each view) and all MUV2 channels (2×22 channels in each view). Energy deposits within 10 ns of the track time are considered; the energy deposit values in every channel or cell are divided by the track momentum.

The GBM algorithms require input information in the form of a single vector for each track. Therefore the LKr, MUV1 and MUV2 energy deposit matrices are transformed into vectors; the LKr matrix is cropped to a size of 18×18 to exploit its sparsity. The results are concatenated into a 588-element feature vector containing the complete information about the track.

The CNN processing aims to exploit the correlations between the LKr, MUV1 and MUV2 signals. Most CNN architectures require an arbitrary number of matrices of identical dimensions (known in the ML context as *channels*) as input. Therefore the LKr, MUV1 and MUV2 matrices are transformed to a fixed size of 44×44 by replicating the element values (though the LKr and MUV matrices correspond to different transverse areas). The resulting matrices are illustrated for two events in Fig. 2. The inputs are finally arranged into a $5 \times 44 \times 44$ input tensor.

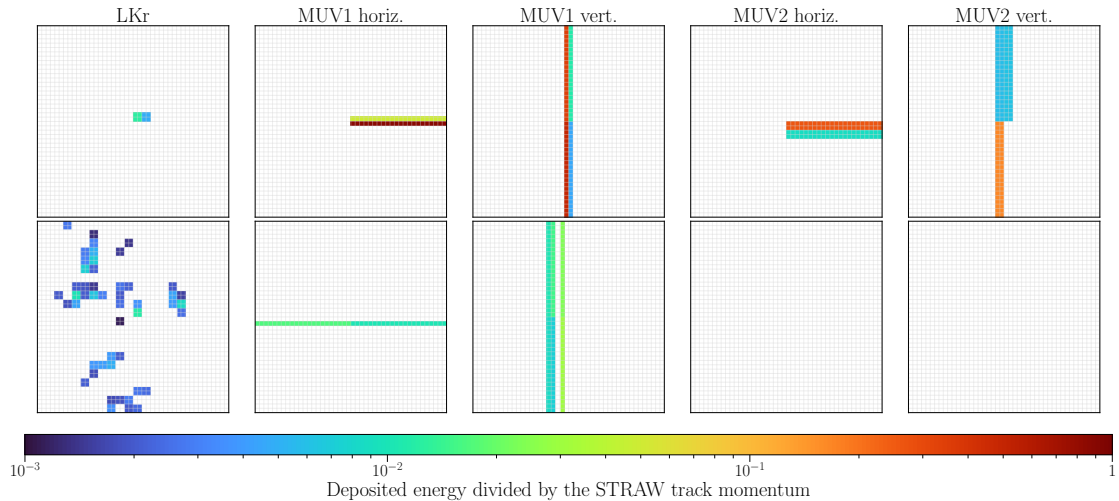


Figure 2: CNN input matrices of 44×44 size constructed for a μ^+ track (top row) and a π^+ track (bottom row) from the training dataset. The LKr matrix is centred at the track impact point in the LKr front plane. In the MUV matrices related to the horizontal (vertical) view, the vertical (horizontal) coordinate is centered at the track impact point in the LKr front plane.

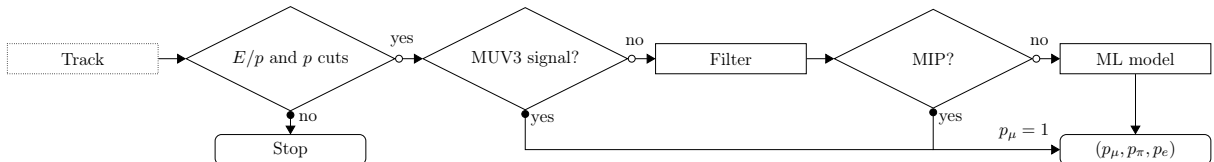


Figure 3: Flow chart of the developed calorimetric PID algorithms.

5 Particle identification algorithm

The flow of the developed PID algorithm is illustrated in Fig. 3. The algorithm returns the probabilities p_π , p_μ , p_e of the track to be classified as π^+ , μ^+ , e^+ , respectively. Tracks with LKr energy deposit to momentum ratio $E/p < 0.95$ are considered, which reduces the e^+ contamination in the π^+ and μ^+ samples. Tracks with matching MUV3 signals, or identified as minimum-ionising particles (MIPs) by a dedicated filter, are assigned $p_\mu = 1$. For the remaining tracks, a ML model (either a GBM or a CNN algorithm) is employed to evaluate the probabilities p_π , p_μ , p_e . The models are trained for tracks in the momentum range 15–40 GeV/c.

Two MIP filter algorithms, which use the same input information as the ML models, are considered. The filter A identifies MIPs as tracks with at most four geometrically associated in-time signals in LKr calorimeter cells, at most two hits in each MUV1 view, and at most one hit in each MUV2 view. The filter B additionally exploits the fact that muons typically produce narrow calorimeter signal patterns. Both ML models have been tested with each of the two filters; the corresponding setups are referred to as GBM/A, GBM/B, CNN/A and CNN/B.

The GBM implementation uses the LightGBM framework, which is efficient for large datasets and high-dimensional feature spaces. A CNN architecture of the ResNet-18 type [14] is used. To handle the sparsely populated input matrices (Fig. 2), the 3×3 maximum pooling layer after the first batch normalisation layer is removed. The network is further simplified by removing the last two residual blocks that include four 512-input convolution layers. The output of the last of the remaining residual blocks is down-sampled via a global average pooling layer, which is followed by a fully connected layer producing the final output subsequently normalised using a softmax function to obtain the probabilities p_π , p_μ and p_e . The resulting NA62ResNet architecture is shown in Fig. 4.

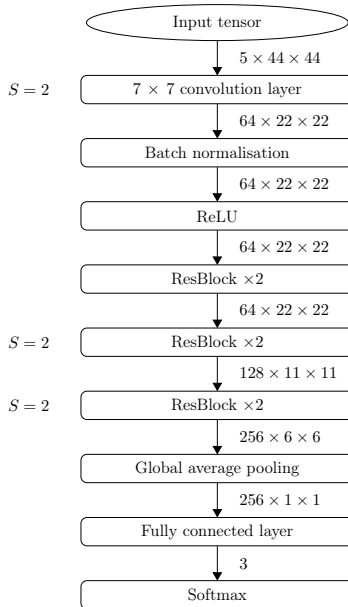


Figure 4: The NA62ResNet architecture. Residual blocks (ResBlock) are stacked in pairs. The stride S [13] is a parameter of the filter. The output tensor dimensions at each step are indicated.

Data augmentation is used to improve the robustness and generalisation of the CNN model: for each epoch of the training, the five input matrices are mirror-imaged with respect to the horizontal axis for 50% of the tracks in the training sample chosen at random. The weights and the bias terms of the fully connected layer are initialised with random numbers distributed uniformly in the $(-1/\sqrt{N}, 1/\sqrt{N})$ range, where $N = 256$ is the number of input features. The convolution layers are initialised using the He scheme [15], and the cross entropy loss function is used. The network parameters are optimised following the Adam method [16]. To detect potential overfitting, the validation loss is monitored during training. The PyTorch framework [17] is used to build and train the model. The architecture is integrated into the NA62 software framework.

The numbers of π^+ , μ^+ and e^+ tracks in the training and validation dataset passing the MIP filter A and used for training (Fig. 3) are 6.9×10^6 , 1.0×10^7 and 7.8×10^4 , respectively. During the model training, 25% of the dataset is randomly set aside to form a validation sample, and the rest is allocated to the training sample. The cross entropy loss function [13] is used for training of both GBM and CNN models.

6 Performance of the algorithm

The results presented in this section are obtained using the test dataset. Background contamination in the π^+ and μ^+ samples in the dataset is found using Monte Carlo simulations to be below 10^{-5} and 10^{-6} , respectively. The p_π distributions for π^+ and μ^+ tracks obtained with the CNN/A setup for tracks in the momentum range of 15–40 GeV/ c are shown in Fig. 5 (left). A condition $p_\pi > p_0$ is used for π^+ identification, where p_0 is chosen for each setup to obtain a π^+ identification efficiency of 75%. The corresponding μ^+ misidentification probabilities, $\varepsilon_{\mu\pi}^{75}$, measured for each setup using a subset of data are displayed in Fig. 5 (right). The CNN/A setup is found to provide the lowest $\varepsilon_{\mu\pi}^{75}$ value, and is used for further analysis. The results reported below are obtained with the CNN/A setup.

The measured $\varepsilon_{\mu\pi}^{75}$ value as a function of track momentum is shown in Fig. 6 (left). Strong μ^+ suppression is achieved also in the momentum range 40–50 GeV/ c not used for training. The receiver operating characteristic (ROC) curve in the momentum range 15–40 GeV/ c is shown

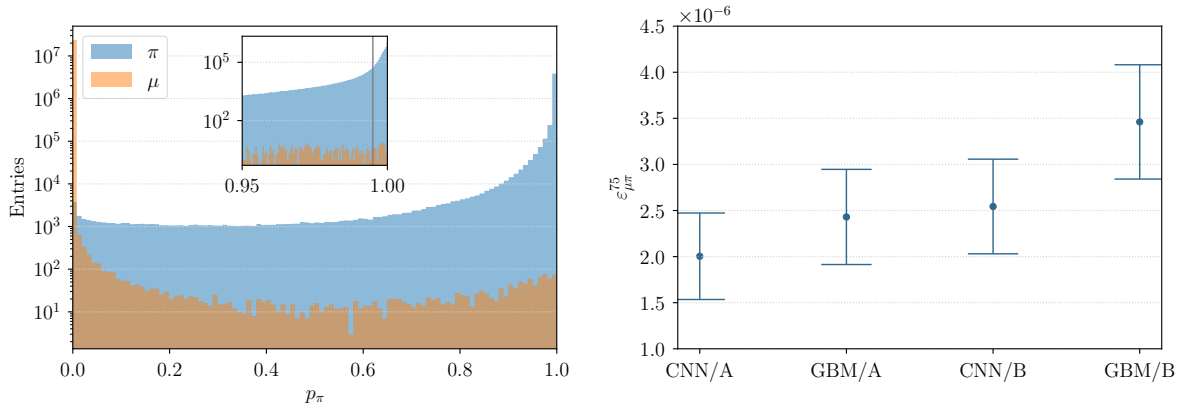


Figure 5: Left: p_π distributions for π^+ and μ^+ tracks in the momentum range of 15–40 GeV/ c obtained with the CNN/A setup for the test dataset. Inset: the high- p_π region; the threshold p_0 chosen for π^+ identification is indicated with a vertical line. Right: μ^+ misidentification probabilities ($\varepsilon_{\mu\pi}^{75}$) with their statistical uncertainties, measured for each setup using a subset of the test dataset.

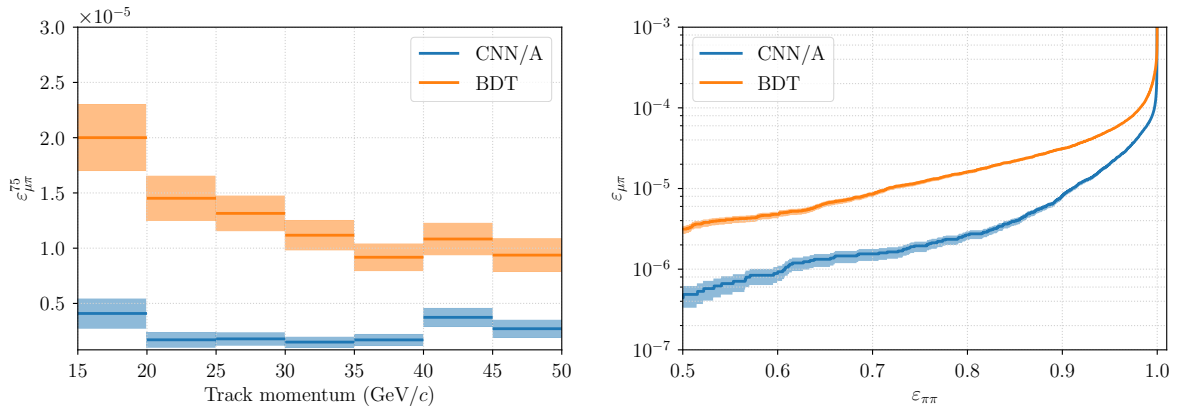


Figure 6: Left: muon misidentification probability ($\varepsilon_{\mu\pi}^{75}$) as a function of track momentum, measured with the CNN/A setup for the test dataset. Right: the ROC curve, i.e. muon misidentification probability ($\varepsilon_{\mu\pi}$) vs pion identification efficiency ($\varepsilon_{\pi\pi}$) for a set of p_0 values, obtained with the CNN/A setup for the test dataset in the 15–40 GeV/ c momentum range. The performance of the BDT algorithm currently used by NA62 is also shown in both panels. The shaded areas represent the statistical uncertainties.

in Fig. 6 (right). An improvement in $\varepsilon_{\mu\pi}^{75}$ by a factor of six, from 1.2×10^{-5} to 2.0×10^{-6} , is obtained with respect to the BDT algorithm currently used by NA62. Alternatively, the π^+ identification efficiency in the above momentum range is increased from 72% to 91% when the muon misidentification probability $\varepsilon_{\mu\pi}$ is kept at a fixed level of 10^{-5} . The e^+ misidentification probability ($\varepsilon_{e\pi}^{75}$) is 35% lower in comparison to the BDT algorithm.

Training the CNN/A model separately in each momentum bin leads to an increase of $\varepsilon_{\mu\pi}^{75}$ by a factor of two across the momentum bins in comparison with Fig. 6, which is attributed to the smaller size and π^+/μ^+ imbalance of the training and validation datasets in the individual bins. Training the model in the entire 15–50 GeV/ c range increases $\varepsilon_{\mu\pi}^{75}$ by about 20% across the momentum bins in comparison with Fig. 6, which is attributed to e^+ contamination in the training and validation dataset above 40 GeV/ c .

7 Summary

A new calorimetric particle identification algorithm based on a convolutional neural network classifier augmented by a filter has been developed for the NA62 experiment at CERN. With respect to the BDT algorithm currently used by NA62, muon misidentification probability as a pion in the momentum range 15–40 GeV/ c is reduced by a factor of six from 1.2×10^{-5} to 2.0×10^{-6} , for a fixed pion-identification efficiency of 75%. Alternatively, pion identification efficiency is improved in the above momentum range from 72% to 91% for a fixed muon misidentification probability of 10^{-5} . The algorithm is applicable to a wide range of NA62 physics analyses, with best performance achieved after careful parameter tuning.

Acknowledgements

The authors are grateful to T. Timbers and the University of British Columbia Master of Data Science Capstone team for their assistance. The authors would also like to thank W. Deng, B. Lie and S. Sethi for their contributions to an early phase of this work. It is a pleasure to express our appreciation to the staff of the CERN laboratory and the technical staff of the participating laboratories and universities for their efforts in the operation of the experiment and data processing.

The cost of the experiment and its auxiliary systems was supported by the funding agencies of the Collaboration Institutes. We are particularly indebted to: F.R.S.-FNRS (Fonds de la Recherche Scientifique - FNRS), under Grants No. 4.4512.10, 1.B.258.20, Belgium; CECI (Consortium des Equipements de Calcul Intensif), funded by the Fonds de la Recherche Scientifique de Belgique (F.R.S.-FNRS) under Grant No. 2.5020.11 and by the Walloon Region, Belgium; NSERC (Natural Sciences and Engineering Research Council), funding SAPPJ-2018-0017, Canada; MEYS (Ministry of Education, Youth and Sports) funding LM 2018104, Czech Republic; BMBF (Bundesministerium für Bildung und Forschung) contracts 05H12UM5, 05H15UMCNA and 05H18UMCNA, Germany; INFN (Istituto Nazionale di Fisica Nucleare), Italy; MIUR (Ministero dell’Istruzione, dell’Università e della Ricerca), Italy; CONACyT (Consejo Nacional de Ciencia y Tecnología), Mexico; IFA (Institute of Atomic Physics) Romanian CERN-RO No. 1/16.03.2016 and Nucleus Programme PN 19 06 01 04, Romania; MESRS (Ministry of Education, Science, Research and Sport), Slovakia; CERN (European Organization for Nuclear Research), Switzerland; STFC (Science and Technology Facilities Council), United Kingdom; NSF (National Science Foundation) Award Numbers 1506088 and 1806430, U.S.A.; ERC (European Research Council) “UniversaLepto” advanced grant 268062, “KaonLepton” starting grant 336581, Europe.

Individuals have received support from: Charles University Research Center (UNCE/SCI/013),

Czech Republic; Ministero dell’Istruzione, dell’Università e della Ricerca (MIUR “Futuro in ricerca 2012” grant RBFR12JF2Z, Project GAP), Italy; the Royal Society (grants UF100308, UF0758946), United Kingdom; STFC (Rutherford fellowships ST/J00412X/1, ST/M005798/1), United Kingdom; ERC (grants 268062, 336581 and starting grant 802836 “AxScale”); EU Horizon 2020 (Marie Skłodowska-Curie grants 701386, 754496, 842407, 893101, 101023808).

References

- [1] E. Cortina Gil et al. “Measurement of the very rare $K^+ \rightarrow \pi^+ \nu \bar{\nu}$ decay”. *JHEP* **06** (2021) 93. arXiv: [2103.15389](#).
- [2] A. J. Buras et al. “ $K^+ \rightarrow \pi^+ \nu \bar{\nu}$ and $K_L \rightarrow \pi^0 \nu \bar{\nu}$ in the Standard Model: status and perspectives”. *JHEP* **11** (2015) 33. arXiv: [1503.02693](#).
- [3] P. Baldi, P. Sadowski, and D. Whiteson. “Searching for exotic particles in high-energy physics with deep learning”. *Nat. Commun.* **5** (2014) 4308. arXiv: [1402.4735](#).
- [4] L. de Oliveira et al. “Jet-images — deep learning edition”. *JHEP* **07** (2016) 69. arXiv: [1511.05190](#).
- [5] P. Baldi et al. “Jet substructure classification in high-energy physics with deep neural networks”. *Phys. Rev. D* **93** (2016) 094034. arXiv: [1603.09349](#).
- [6] G. Ke et al. “LightGBM: A Highly Efficient Gradient Boosting Decision Tree”. *NIPS* 2017.
- [7] J. H. Friedman. “Greedy function approximation: a gradient boosting machine”. *Ann. Stat.* **29.5** (2001) 1189.
- [8] A. Höecker et al. “TMVA: Toolkit for Multivariate Data Analysis”. *PoS ACAT* (2007) 040. arXiv: [physics/0703039](#).
- [9] E. Cortina Gil et al. “The beam and detector of the NA62 experiment at CERN”. *JINST* **12** (2017) P05025. arXiv: [1703.08501](#).
- [10] R. Ammendola et al. “The integrated low-level trigger and readout system of the CERN NA62 experiment”. *Nucl. Instrum. Methods A* **929** (2019) 1. arXiv: [1903.10200](#).
- [11] E. Cortina Gil et al. “Performance of the NA62 trigger system”. *JHEP* **03** (2023) 122. arXiv: [2208.00897](#).
- [12] I. Goodfellow, Y. Bengio, and A. Courville. “Deep Learning”. MIT Press, 2016.
- [13] K. P. Murphy. “Probabilistic Machine Learning: An introduction”. MIT Press, 2022.
- [14] K. He et al. “Deep residual learning for image recognition”. *CVPR* 2016. arXiv: [1512.03385](#).
- [15] K. He et al. “Delving Deep into Rectifiers: Surpassing Human-Level Performance on ImageNet Classification”. *ICCV* 2015. arXiv: [1502.01852](#).
- [16] D. P. Kingma and J. Ba. “Adam: A method for stochastic optimization”. *ICLR* 2015. arXiv: [1412.6980](#).
- [17] A. Paszke et al. “PyTorch: An Imperative Style, High-Performance Deep Learning Library”. *NeurIPS* 2019. arXiv: [1912.01703](#).